



**Queensland University of Technology**  
Brisbane Australia

This may be the author's version of a work that was submitted/accepted for publication in the following source:

[McCosker, Audrey B., Snowdon, Mikayla E., Lamont, Riki, Woodruff, Maria A., & Paxton, Naomi C.](#)

(2022)

Exploiting Nonlinear Fiber Patterning to Control Tubular Scaffold Mechanical Behavior.

*Advanced Materials Technologies*, 7(11), Article number: 2200259.

This file was downloaded from: <https://eprints.qut.edu.au/233996/>

© 2022 The Authors

This work is covered by copyright. Unless the document is being made available under a Creative Commons Licence, you must assume that re-use is limited to personal use and that permission from the copyright owner must be obtained for all other uses. If the document is available under a Creative Commons License (or other specified license) then refer to the Licence for details of permitted re-use. It is a condition of access that users recognise and abide by the legal requirements associated with these rights. If you believe that this work infringes copyright please provide details by email to [qut.copyright@qut.edu.au](mailto:qut.copyright@qut.edu.au)

**License:** Creative Commons: Attribution 4.0

**Notice:** *Please note that this document may not be the Version of Record (i.e. published version) of the work. Author manuscript versions (as Submitted for peer review or as Accepted for publication after peer review) can be identified by an absence of publisher branding and/or typeset appearance. If there is any doubt, please refer to the published source.*

<https://doi.org/10.1002/admt.202200259>

# Exploiting Nonlinear Fiber Patterning to Control Tubular Scaffold Mechanical Behavior

Audrey B. McCosker, Mikayla E. Snowdon, Riki Lamont, Maria A. Woodruff, and Naomi C. Paxton\*

Melt electrowriting is an additive manufacturing technique capable of fabricating highly biomimetic polymer scaffolds with high-resolution microarchitecture for a range of tissue engineering applications. The use of a rotating mandrel to fabricate tubular scaffolds using this technique is increasing in popularity; however, the translation of many novel scaffold designs that have been explored on flat collectors has yet to be realized using mandrels. This study reports novel tools to automatically generate scaffold gcode for several new tubular scaffold designs, investigating a range of auxetic pore geometries and open unit cell designs. Through optimization of printing parameters, the novel scaffold designs are successfully printed and mechanically tested to assess tensile properties. Open unit cells significantly reduce the tensile stiffness of scaffolds manufactured with closed pores. Auxetic scaffolds could also be widely tuned using the novel gcode generator tool to exhibit similar stress–strain profiles to typical crosshatch scaffolds but could be made to expand to desired radial dimensions. Finally, heterogeneous auxetic constructs are also fabricated with regions of various radial compliances. This study presents several, mechanically validated novel scaffold designs that are of interest for future applications in targeted tissue engineering product development as well as in soft robotic actuation.


## 1. Introduction

Melt electrowriting (MEW) is an additive manufacturing method providing researchers with a unique technical capability to fabricate microfiber tubular scaffolds with a high level of control over scaffold architecture, unachievable with typical 3D printing approaches.<sup>[1]</sup> This technique has emerged in tissue engineering and biofabrication research over the last decade and received

considerable interest for producing tubular scaffolds, by extruding micron-scale fibers onto a rotating mandrel, for a variety of tissue engineering applications.<sup>[2,3]</sup> MEW relies on the pressure-driven extrusion of molten polymers or polymer composites through a nozzle onto a computer-controlled collector.<sup>[4]</sup> The application of a high potential difference between the nozzle and collector instigates Taylor cone formation and the generation of a jet which is up to an order of magnitude smaller in diameter than the nozzle.<sup>[5]</sup> By depositing fibers on a rotating mandrel with linear slide translation, tubular structures of wide-ranging diameters can be fabricated using different sized mandrels, ranging from mm- to cm-scale as well as incorporating the use of molds for personalized, anatomical tubular scaffold morphology.<sup>[2]</sup> A strong focus of MEW has been on designing scaffold geometries optimized for wide ranging tissue engineering applications to ensure mechanical matches between the regenerated tissues and targeted biomechanical environment.<sup>[6]</sup>

While a substantial volume of research has focused MEW scaffolds printed on flat plates, the development of tubular MEW scaffolds has undergone incremental improvement since the initial reports of using MEW to print onto rotating mandrels.<sup>[7]</sup> Tubular scaffold fabrication was initially limited to simple mesh-like structures, which have demonstrated substantial promise in applications such as long bone tissue engineering,<sup>[8]</sup> but lacked the nuanced “writing” functionality unique to MEW to fabricate structures with controlled and variable microarchitecture.<sup>[9]</sup> However, with the development of gcode generation tools, scaffolds with well-defined, ordered crosshatch or diagonal pores could be fabricated.<sup>[10,11]</sup> Many studies still rely on the use of a constantly rotating mandrel in a single direction to achieve scaffolds with crosshatch architecture.<sup>[3,12]</sup> Only more recently have novel scaffold designs been proposed exploiting stepper motor functionality to maneuver more complex patterns on the rotating radial axis in conjunction with linear translation.<sup>[6,13,14]</sup> The recent implementation of more advanced hardware on custom MEW machines to control mandrel rotation with the same precision as XY-axis printers has driven the development of more complex scaffold architectures.

A. B. McCosker, M. E. Snowdon, R. Lamont, M. A. Woodruff, N. C. Paxton  
Centre for Biomedical Technologies (CBT)  
Queensland University of Technology (QUT)  
60 Musk Ave, Kelvin Grove, QLD 4059, Australia  
E-mail: n.paxton@qut.edu.au

 The ORCID identification number(s) for the author(s) of this article can be found under <https://doi.org/10.1002/admt.202200259>.

© 2022 The Authors. Advanced Materials Technologies published by Wiley-VCH GmbH. This is an open access article under the terms of the Creative Commons Attribution License, which permits use, distribution and reproduction in any medium, provided the original work is properly cited.

DOI: 10.1002/admt.202200259

In parallel to the incremental advancements in MEW hardware to achieve tubular scaffolds, research has focused on improving the ability to rapidly design and program scaffold architectures using gcode, which is the coordinate-based programming language used to control MEW scaffold fabrication. It is well known that a major drawback of using MEW is the restriction presented by having to use a constant fiber jet to manufacture scaffolds in one continuous thread. This poses challenges for designing scaffolds, both on a flat plate and rotating mandrel, since most commercial software is not well-suited to the nuances of MEW.<sup>[11,15]</sup> Thus, researchers have developed proprietary software tools to input desired scaffold design parameters and automatically generate the corresponding gcode. However to date, these have been limited to simple crosshatch designs<sup>[10]</sup> which are known to have limited biological relevance. MEW research for flat-plate scaffolds are moving toward more biomimetic designs;<sup>[15–17]</sup> however, limited designs have been translated to mandrel fabrication for tubular scaffolds. Furthermore, the use of a rotating mandrel to produce tubular scaffolds limits the design freedom for creating homogeneous porous scaffolds, since the number of pores around the scaffold circumference should ideally be an integer as to not introduce radial inhomogeneity or discontinuity, and potential sources of mechanical failure. This critically limits the ability to design scaffolds with specific pore geometries as they must fit within the circumference of the scaffold and enable constant fabrication along the length of the scaffold.<sup>[18]</sup> Finally, lead-in regions around the periphery of flat-plate scaffolds have been widely used to accommodate the often-inaccurate deposition of the fibers around sharp corners.<sup>[19]</sup> However, for tubular scaffolds, there exists only opportunity for jet correction and “turn-around” zones in the X axis, where the  $\omega$  circumferential plane acts as a continuous surface. These restrictions pose additional challenges in the ability to design more complex patterns and develop software tools to automate this design process for rapid iteration of scaffold development.

Finally, tuning the MEW jet itself plays a critical role in the development of scaffolds with complex architecture. Several studies have investigated various aspects of the MEW process and its impact on accurate fiber deposition. Prior work has investigated the critical translation speed (CTS) which informs the speed at which the fiber is deposited in a perfectly straight line required for MEW compared to electrospinning.<sup>[4,5,20]</sup> Whilst it is routine to compromise on speed to achieve more rapid scaffold fabrication, particularly in instances where lead-in regions around the periphery of the required scaffold area are removed prior to analysis, the CTS must be strictly employed to fabricate high resolution structures with small features.<sup>[21]</sup> More recent studies have further investigated methods to correct for the lag in the jet to achieve uniform wave-like structures with uniform amplitude at increasing height<sup>[15]</sup> as well as bespoke fiber stacking geometries.<sup>[22]</sup> These jet dynamic phenomena present substantial challenges in realizing the accurate fabrication of tubular structures to translate novel tubular scaffold architectures with tunable mechanical properties suited to various native tissues into manufacturable products.

The aim of this research is to propose a suite of novel tubular scaffold geometries for fabrication via MEW with controllable pore geometry and tunable mechanical properties that have not

yet been explored in the literature. Furthermore, we report for the first time the automatic generation of widely tunable auxetic patterns for expandable tubular scaffolds, alongside “brick-like” patterns that enable open unit cell designs to augment tensile and bending properties. The incorporation of straight versus radial fibers is explored to replicate popular scaffold architectures proposed in the literature and clinical products to instigate radial elasticity and compliance in vivo.<sup>[15,23]</sup>

## 2. Results and Discussion

### 2.1. Nonlinear Scaffold Design and Fabrication

Several novel scaffold designs were conceptualized to demonstrate the use of nonlinear fibers to generate scaffolds with tunable mechanical behavior compared to the widely used crosshatch pattern with diamond-shaped pores (Table 1).<sup>[10,11]</sup> A re-entrant honeycomb unit cell pattern was selected for auxetic expandable scaffolds (Figure S1),<sup>[24,25]</sup> whilst a brick-like structure was proposed to compare the mechanical behavior of open pores compared to a closed-pore alternative (Table 1).

Scaffold geometries were computed using a custom MATLAB script to calculate unit cell dimensions based on input parameters controlling the scaffold geometry which then generated coordinate commands in the form of gcode. To determine a suitable printing path, several criteria were established to ensure accurate, reproducible fabrication. First, where possible, linear fibers were preferred instead of piece-wise fibers to decrease the number of shorter fiber segments and turns within the scaffold pattern between ends. This could be achieved for 100% of fibers in the diamond pattern, as the simplest and most widely studied scaffold design. Similarly, concentric straight or wavy fibers were printed in succession for the closed cell design scaffolds, followed by sequential fibers

**Table 1.** Six scaffold designs proposed in this study, including a description of the pore geometry, abbreviated name and design inputs controlling the architecture of each scaffold.

No.	Scaffold Design Name	Abbreviated Name	Design Inputs <sup>a)</sup>
1	Diamond	<i>Diamond</i>	<ul style="list-style-type: none"> <li>• Pore Area (mm<sup>2</sup>)</li> <li>• Pore Angle (°)</li> </ul>
2	Auxetic Re-entrant Honeycomb	<i>Auxetic</i>	<ul style="list-style-type: none"> <li>• Radial Strain (%)<sup>b)</sup></li> <li>• Longitudinal Strain (%)<sup>b)</sup></li> </ul>
3	Closed Unit Cell with Straight Radial Fibers	<i>Closed Cell (straight)</i>	<ul style="list-style-type: none"> <li>• Pore width (mm)</li> <li>• Pore radial height (mm)</li> </ul>
4	Closed Unit Cell with Wavy Radial Fibers	<i>Closed Cell (wavy)</i>	<ul style="list-style-type: none"> <li>• Pore width (mm)</li> <li>• Pore radial height (mm)</li> <li>• Wave amplitude (mm)</li> </ul>
5	Open Unit Cell with Straight Radial Fibers	<i>Open Cell (straight)</i>	<ul style="list-style-type: none"> <li>• Pore width (mm)</li> <li>• Pore radial height (mm)</li> </ul>
6	Open Unit Cell with Wavy Radial Fibers	<i>Open Cell (wavy)</i>	<ul style="list-style-type: none"> <li>• Pore width (mm)</li> <li>• Pore radial height (mm)</li> <li>• Wave amplitude (mm)</li> </ul>

<sup>a)</sup>In addition to scaffold length, diameter (mandrel size) and number of layers;

<sup>b)</sup>Strain at which the unit cell is completely unfolded.

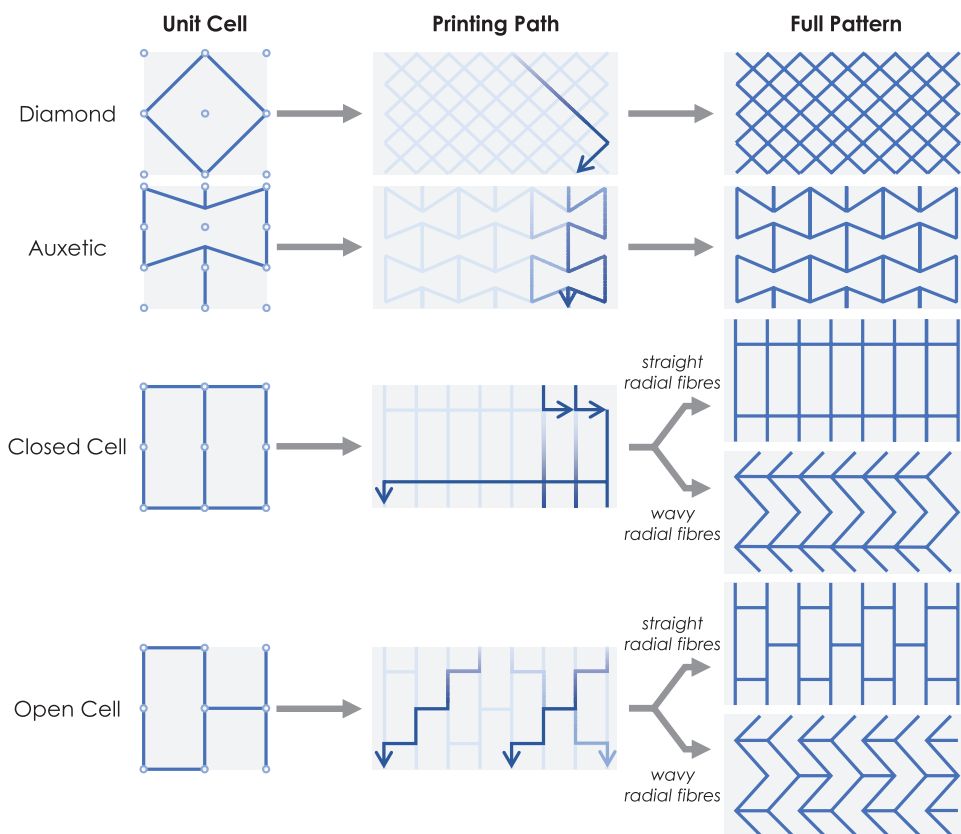


**Figure 1.** Schematic overview of the scaffold designs proposed in this study: diamond (crosshatch), auxetic, closed unit cell with both straight and wavy radial fibers, and open unit cell with both straight and wavy radial fibers. The individual repeating unit cell is shown, alongside a schematic of the developed printing path and final full scaffold pattern.

traveling along the length of the scaffold to complete the closed cell design. However, for the auxetic and open cell designs, the prevalence of nodes with an odd number of intersecting fibers were common, thus limiting the ability to fabricate structures without using nonlinear or overlapping fibers. Therefore second, a preference was given to ensuring constant rotation of the mandrel in a single direction, to limit the prevalence of jet lag-induced printing errors between layers printed in different directions.

Using these criteria, a printing path for the auxetic pattern was developed by printing consecutive radial “columns” of zig-zagging fibers (**Figure 1**), resulting in the double-up of fibers printed along the vertical struts oriented around the circumference of the scaffold and thus, non-load-bearing in the tensile regime. Similarly, the open cell design was constructed using several passes back and forth along the scaffold length to complete the entire pattern, resulting in each iteration of the entire pattern consisting of 3 layers of fibers.

Gcode was then developed for each pattern, using a relative coordinate system to generate commands for fabricating each scaffold design with the desired pore size and number of layers. Micrographs of the printed scaffolds are shown in **Figure 2**. The predominantly linear geometries (diamond & closed cell with straight fibers) were fabricated with a high degree of precision, with no visible defects in fiber alignment or stacking observed in the micrographs. However, minor defects are visible in

scaffolds with more complex geometry, particularly during large changes in direction during printing, or junctions with multiple overlapping fibers in several directions (open cell designs). Importantly, no significant difference in fiber diameter was observed since the print parameters were consistently maintained during the fabrication of all scaffolds (**Figure S2**).

These printing inaccuracies are a well-studied phenomenon in MEW research, relating to the build-up of charge in deposited fibers and subsequent electrostatic interactions between them and the new fibers being deposited on top.<sup>[22]</sup> These challenges are exacerbated by the nonlinearity of fibers, resulting in nonhomogeneous deflection of deposited fibers around areas of tight direction change and intersecting fibers during successive layer fabrication. Tuning the printing parameters to achieve fabrication at the critical translation speed (CTS) was therefore crucial to ensure that the patterns could be produced with as high accuracy as possible, requiring the jet lag to be as small as possible, without printing below the CTS where the fiber may buckle and overshoot the intended geometric design. This optimization was achieved through systematic observation of scaffold morphology across a range of printing speeds and voltages (**Figure S3**) until the most optimal combination of parameters was selected to achieve high quality, reproducible scaffolds. Here, 4.5 kV and 400 mm/sec were selected as the optimal combination of high voltage and collector speed.

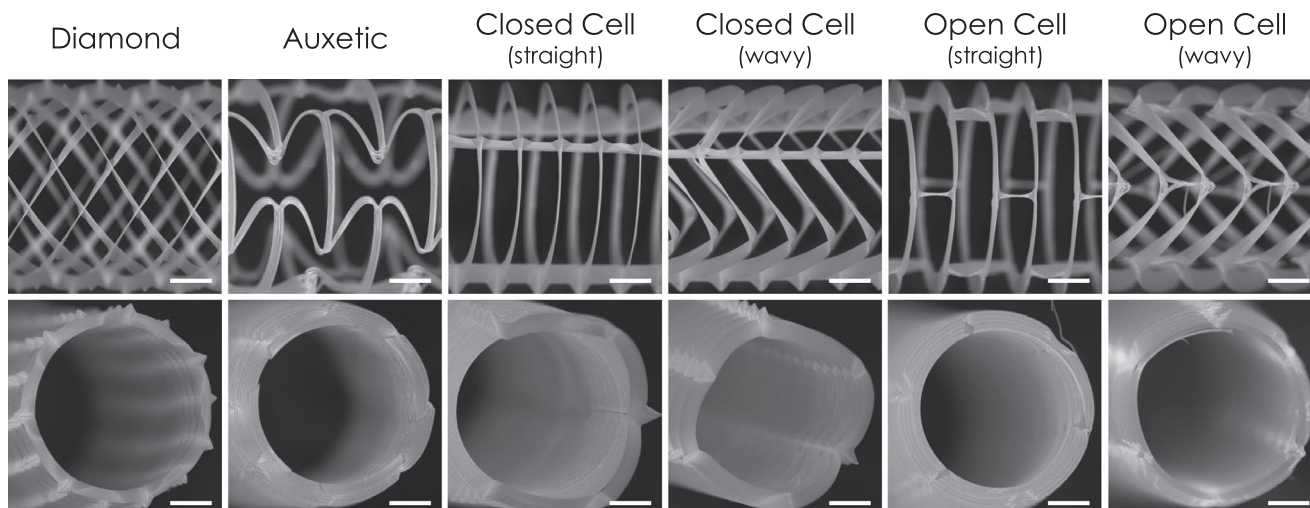


**Figure 2.** Micrographs of printed tubular scaffolds for each of the six patterns developed in this study. Scale bar = 2 mm.

## 2.2. Scaffold Mechanical Behavior with Tensile Loading

The behavior of the scaffolds undergoing tensile mechanical loading was investigated by comparing the stress–strain

curves (Figure 3a), Young's modulus (Figure 3b) and visualization of the scaffolds during tensile testing (Figure 3c). Images were captured of each scaffold during tensile loading before testing (0), as well as during the three observed stages

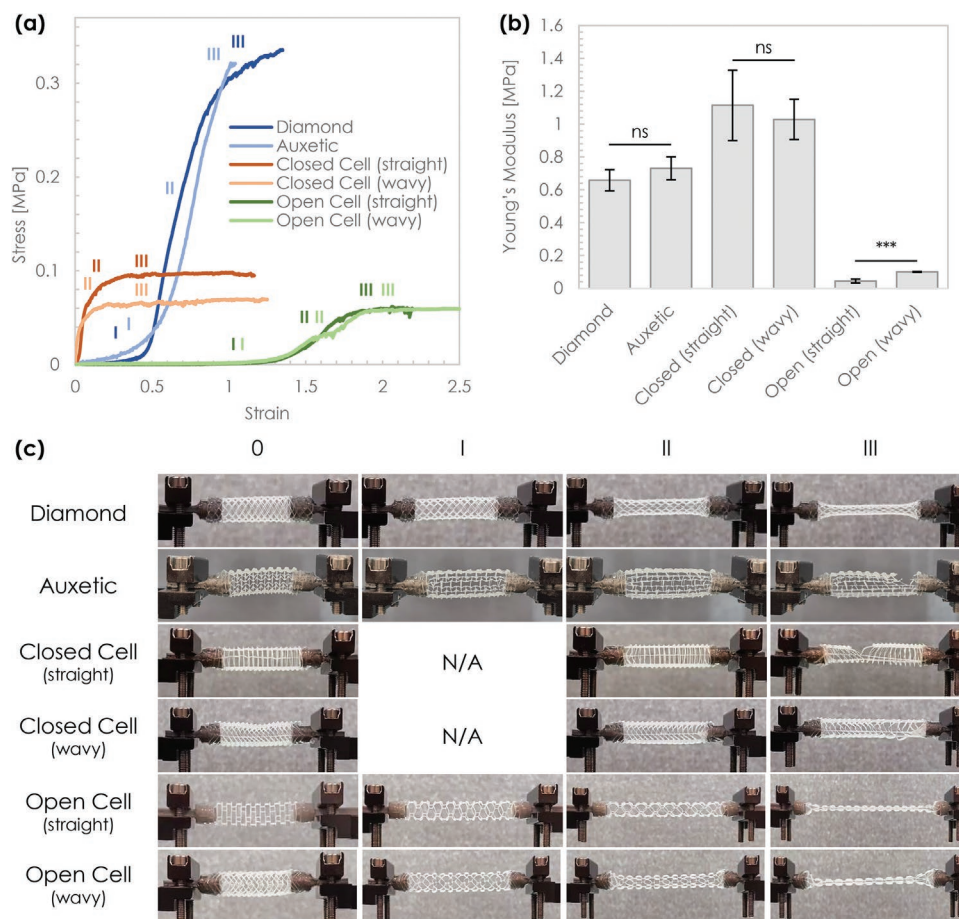


**Figure 3.** Mechanical behavior of MEW tubular scaffolds with varying pore design. a) Representative stress–strain profiles for each scaffold design. b) Young's modulus for each scaffold design, reported as average  $\pm$  SD ( $n = 4$ ), \*\*\*  $p < 0.001$ , n.s. = nonsignificant. c) Representative images of scaffolds prior to testing (0), during the I) toe region, II) linear elastic region, and III) plateau region of the stress strain profiles, as indicated in (a).

of deformation: (I) toe region of the stress–strain curve corresponding to the scaffold pores elastically deforming, (II) the linear elastic region of the stress–strain curve corresponding to the loading of the scaffold fibers, and (III) the plateau region of the stress–strain curve corresponding to the plastic deformation of the scaffold fibers and delamination of the printed construct. Given the vastly different tensile behavior of the scaffolds, representative images were selected based on the stress–strain curve for each scaffold design and therefore occurred at different strains, as indicated by the markers in Figure 3a.

Given the similarity in pore size and porosity between the diamond auxetic scaffolds, similar stress–strain profiles were observed with no significant difference between the elastic moduli for each scaffold design (Figure 3a,b). This is consistent with previous studies demonstrating the ability to achieve near-identical stress strain behavior between these scaffolds, despite opposite Poisson’s ratios.<sup>[14]</sup> Accordingly, expansion of the auxetic scaffolds were observed, demonstrating their negative Poisson’s ratio (NPR) whilst the diamond scaffold exhibited radial contraction (Figure 3c).

A significant difference in mechanical properties was observed between the closed and open unit cell design scaffolds. As anticipated, the closed unit cell designs exhibited an order-of-magnitude higher stiffness than the open unit cell design due to the inclusion of continuous longitudinal fibers along the length of the scaffold. These fibers were immediately loaded and no pore deformation, nor toe region in the stress–strain curve, was observed (Figure 3a,b), contributing to early failure compared to the other scaffolds with deformable pore geometries (Figure 3). The open unit cells conversely allowed significant longitudinal deformation of the scaffold, exhibited by the toe region extending up to  $\approx 150\%$  strain as the open pores were stretched (Figure 3a,c). The offset design of the fibers parallel to the loading axis (indicated by vertical lines in Figure 1) in the open cell scaffolds therefore significantly decreased the stiffness of the scaffolds and increased their longitudinal elasticity

compared to the closed cell scaffolds with continuous straight fibers along the length of the scaffold.

As expected, the inclusion of wavy radial fibers did not substantially vary the tensile behavior of the closed and open cell scaffold designs. Since the tensile load was imparted through fibers parallel to the loading axis, the added radial elasticity exhibited by the wavy closed and open cell scaffolds played an insignificant role in augmenting the mechanical properties of the scaffolds. As such, no significant difference in the Young’s modulus was observed between the straight and wavy closed unit cell designs (Figure 3b). A small difference was observed between the straight and wavy open unit cell designs. However, this was likely due to printing error marginally reinforcing some of the fiber junctions to instigate slight additional stiffness (Figure 3b). Overall, the mechanical behavior of MEW scaffolds could be readily tuned through use of auxetic, closed and open unit cell designs.

### 2.3. Unit Cell Design Informs Mechanical Behavior

To illustrate the versatility of changing the pore geometry, the auxetic scaffold design was selected to explore the influence of pore geometry on mechanical properties, given the interesting NPR behavior of the auxetic unit cell design. Here, auxetic scaffolds with a range of unit cell geometries were programmed based on their predicted strain at the point at which the unit cell was completely unfolded, termed “maximum strain” in the radial and longitudinal axes. Sixteen scaffold geometries were designed and fabricated, programmed to expand to 25%, 50%, 75%, and 95% radial expansion, and 25%, 50%, 75%, and 100% longitudinal strain for the unit cell to completely unfold (Figure 4a).

To instigate increasing maximum radial strain achievable with unfolding pores, the diagonal fibers comprising the bow-tie-like auxetic pore shape increased in length and the spacing between diagonal fibers decreased. In parallel, to

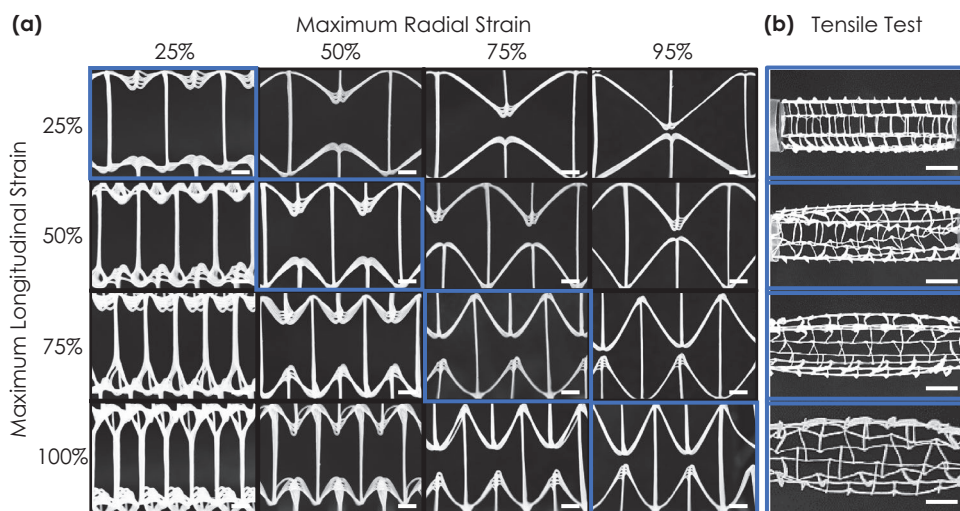


**Figure 4.** a) Micrographs of a suite of auxetic MEW tubular scaffolds with varying pore geometry ranging from 25–100% increase in strain to completely unfold the unit cells. Scale bars = 1 mm. b) Representative images from tensile testing of four scaffold geometries indicated by blue borders in (a) during tensile testing, at the point of maximum longitudinal strain and corresponding radial expansion. Scale bars = 5 mm.

achieve increasing longitudinal strain over which the unit cell unfolds, the unit cell width was compressed, offering greater opportunity for elastic unfolding of the bow-tie-like shape to a rectangular shape (Figure 4b). Using the desired mechanical behavior as input properties, this study offers a novel approach to automatic scaffold gcode design to immediately fabricate scaffolds with targeted mechanical behavior suitable for various applications in tissue engineering, biofabrication and soft robotics; overcoming the highly iterative and time-consuming traditional approach to scaffold design by first selecting geometry-driven parameters before assessing their impact on mechanical properties.

## 2.4. Heterogeneous Scaffold Design

With the ultimate goal of many tissue engineering strategies being to closely replicate the anatomical structure and function of tissues,<sup>[26,27]</sup> a novel component of the gcode generator was developed to enable rapid design of scaffolds with nonhomogeneous mechanical properties. By defining the desired radial and longitudinal expansion of two or more regions along a tubular scaffold, heterogeneous scaffolds were designed which could be tuned to conform to anatomical structures or impart nonuniform radial tension to reinforce tubular structures in desired locations in the body. **Figure 5** depicts an example heterogeneous auxetic scaffold with three defined regions of pore geometry to instigate radial expansion of 50%, 95%, and 75% maximum radial strain respectively (Figure 5a). Under tensile loading, the scaffold accordingly expanded to different final diameters, indicated by the arrows (Figure 5b).

“Edge effects” were present while imaging auxetic scaffolds during tensile loading, due to the fixed mounting points of the scaffold which did not accommodate for radial expansion. Thus, expansion at the edges of the scaffold, as well as at the intersections between regions with different maximum radial

strain exhibited a curvature of the outer edge of the scaffold. As such, care was taken to program the asymmetrical pores to transition for each region of varying pore geometry. The transition pores are indicated in Figure 5c where the pores were programmed to blend the required pore geometries from each adjacent region. Figure 5c-i) depicts the transition between the pores with 50% radial expansion to 95% radial expansion, with the according elongation of the diagonal re-entrant fibers and decrease in spacing between diagonal fibers in the center of the pore, while Figure 5c-ii) depicts the transition from the 95% radial expansion region to 75% radial expansion region and corresponding augmentation of the pore geometry. This ensured the auxetic pattern was continuously printed across the scaffold without any discontinuity of the pattern which may result in more significant edge effects, defects or other inconsistency impacting mechanical performance. For this heterogeneous scaffold, the tensile testing results exhibited a smooth J-shaped stress–strain curve characteristic of the homogeneous auxetic scaffolds (Figure 5d).

This scaffold design tool offers the unique ability to fabricate nonhomogeneous mechanical regions via a continuous auxetic pattern across the tubular scaffold with no break in scaffold geometry, delineation between regions or extraneous overlapping fibers during the transition from regions of varying scaffold morphology. Importantly, it enables us to instigate targeted design features to enable varied mechanical behavior within a single scaffold. This may be of significant interest for the future development of heterogeneous scaffolds for applications in cardiovascular tissue engineering, including for vascular grafts, aortic root and heart valve applications where radial compliance is of critical importance to the success of surgical interventions. As the emergence of fiber-reinforcement for soft robotic applications continue to evolve,<sup>[28]</sup> microfibre scaffolds have demonstrated utility in augmenting the deformation of soft robotic actuators. Leveraging the unique ability of MEW to customize and tailor the mechanical behavior of scaffolds, targeted and highly controllable tensile and bending regimes

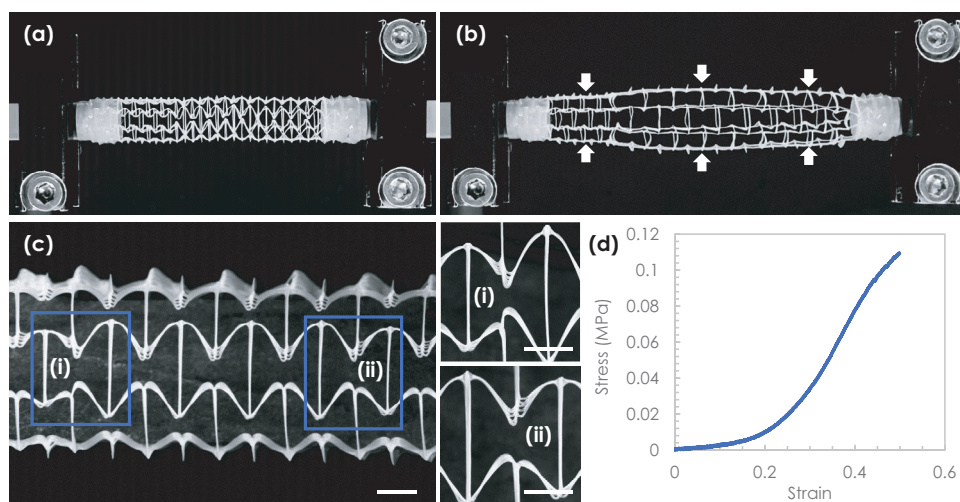


**Figure 5.** A tubular MEW scaffold designed with three regions of auxetic pore geometry to achieve heterogeneous expansion. Images of the scaffold a) before and b) during tensile mechanical testing to verify radial expansion of the three regions (white arrows). c) Micrograph of the tubular scaffold with transitional pores designed to accommodate the change in geometry between regions, as indicated by close-up images i) and ii). Scale bars = 2 mm. d) Stress–strain curve for the heterogeneous auxetic scaffold during tensile loading.

may be achievable using scaffold designs demonstrated in this study. Heterogeneous scaffold design may also provide valuable avenues to rapidly expedite the development of targeted soft robotic actuation.

### 3. Conclusion

This study has reported the development of novel MEW scaffold designs and demonstrated the ability to customize, optimize and control the mechanical properties of MEW scaffolds through the use of auxetic and open-cell designs compared to well-known closed-cell crosshatch structures. It was found that open unit cell designs, exploiting a newly developed fiber lay-down path for the fabrication of a “brick-like” pattern using continuous MEW fiber generation, enabled the ability to massively tailor the tensile properties of MEW scaffolds by an order of magnitude. This substantial tunability of scaffold mechanical properties was emulated in an auxetic unit cell design which enabled the selection of the maximum strain reached during unfolding of the unit cell designs, both in longitudinal strain and radial expansion. Furthermore, heterogeneous MEW scaffolds comprising several regions of varying pore sizes manufactured as a single, continuous scaffold were demonstrated. Overall, this study has expanded the library of available gcode generation tools and fiber patterning options for MEW scaffold design toward the development of precision microfiber scaffolds with tailorable and tunable mechanical properties, in different regions of the scaffold, for wide-reaching applications in tissue engineering, biofabrication, and soft robotics.

### 4. Experimental Section

**Materials:** Polycaprolactone (PCL) pellets were purchased from Sigma-Aldrich ( $M_w = 45$  kDa).

**Scaffold Design:** Scaffolds with complex pore geometries were designed by first identifying the repeating unit cell structure, and then repeating the pattern across a 2D plane corresponding to the length and circumference of the tubular scaffold. The six scaffold geometries described in Table 1 comprise the following parameters: 40 mm length, 15 layers and pores with uniform fiber spacing of 2 mm longitudinal spacing and 4.18 mm radial spacing. The diamond patterned tubular scaffold design is used widely in the scientific literature and was fabricated as a control group with a 93° laydown angle (exactly 90° results in a scaffold with a noninteger number of pores around the circumference.<sup>[11]</sup> Auxetic scaffolds were designed using a re-entrant honeycomb pattern with the same external scaffold dimensions, and with a range of pore sizes corresponding to their ability to expand longitudinally and radially to programmed strains ranging from 25–100% via equations supplied in Figure S1 (Supporting Information). Scaffold geometries were computed using a custom MATLAB script to calculate unit cell dimensions based on input parameters controlling the scaffold geometry and then generated coordinate commands following the printing paths graphical depicted in Figure 1 in the form of gcode.

**Melt Electrowriting (MEW):** Scaffolds were fabricated using a custom-built MEW device described previously<sup>[11]</sup> fitted with a rotating stainless-steel mandrel, 8 mm in diameter. PCL pellets were placed in a 2 mL syringe (B. Braun, Australia) with a 21 G blunt tip needle (Nordson, USA) and melted in a custom heating jacket with the temperature set at 90 °C, for 15 min, and stabilized for a further 15 min prior to printing. A regulated air pressure (SMC, Japan) at 0.08 MPa was applied to the syringe and 4.5 kV high voltage was applied to the rotating mandrel

collector while the needle was grounded. The working distance between the tip and rotating mandrel was maintained at a constant distance of 3 mm and fibers were deposited on the rotating mandrel and 4-axis collector system (Velmex, USA) controlled by Repetier Host software (Hot-World GmbH & Co. KG, Germany) at a constant speed of 400 mm min<sup>-1</sup>. Printing was performed under ambient conditions (21.0 ± 0.4 °C, 52% relative humidity).

Five replicates of each scaffold of the six scaffold geometries (diamond, auxetic, closed cell with straight or wavy radial fibers, and open cell with straight or wavy radial fibers) were printed for mechanical testing and imaging. An additional four replicates of 16 different auxetic patterns were fabricated with programmed maximum radial expansion of 25%, 50%, 75%, and 95%, and maximum longitudinal expansion of 25%, 50%, 75%, and 100% at the tensile strain at which the unit cell is completed unfolded. Following fabrication, the printed structures were carefully removed from the mandrel using ethanol and stored for imaging and mechanical testing.

**Tensile Testing:** Tensile testing was performed to visualize scaffold deformation during tensile loading and to quantify the Young's modulus of the scaffolds. Scaffolds were adhered to custom 3D printed mounts described previously,<sup>[11,14]</sup> which featured a rectangular prism (7.3 × 3.3 × 20 mm) for attaching within the mechanical testing grips, connected to a cylinder (8 mm  $\phi$ , 8 mm depth) onto which the scaffold is affixed using epoxy (Selleys Araldite, 2-Part Quick Set). A thin coating of epoxy,  $\approx$ 1 mm in thickness, was applied to the cylindrical surface of the mount before it was inserted into the end of the scaffolds, overlapping by  $\approx$ 5 mm. Once the epoxy had set, the scaffolds were then mounted onto a tensile testing system (Tytron 250 Microforce Testing System (MTS), MTS Systems Corp, USA) with 250 N load cell calibrated at  $\pm$ 25 N with 2.5 mN resolution. Loading was undertaken at 1 mm s<sup>-1</sup> and force-displacement data was recorded. Stress-strain analysis was undertaken on tensile profiles, where the cross-sectional area of each scaffold was presumed to be the difference between inner and outer diameter of the scaffold. While not considering scaffold porosity, this is a widely used assumption when evaluating the mechanical properties of porous scaffolds.<sup>[15,29]</sup>

**Scaffold Imaging:** Scaffolds were imaged using a stereomicroscope (SMZ25, Nikon, Japan) as well as using a smartphone camera (Samsung S20, South Korea) to visualize overall geometry and pore morphology. ImageJ was then used to measure fiber diameter in replicate ( $n = 5$ ).<sup>[30]</sup>

**Statistical Analysis:** Measurements performed in replicate were reported as average  $\pm$  standard deviation (SD). Significance between experimental groups was calculated using a one-way ANOVA and Student's *t*-test, where  $p < 0.05$  was considered significant.

### Supporting Information

Supporting Information is available from the Wiley Online Library or from the author.

### Acknowledgements

A.B.M. and M.E.S. contributed equally to this work. The authors gratefully acknowledge technical assistance from Ms. Elizabeth Graham (mechanical testing) and Dr. Kah Meng Lee (imaging). The data reported were obtained using the resources of the Central Analytical Research Facility within the Research Infrastructure Division, Queensland University of Technology, with funding from the Faculty of Engineering. NC Paxton is supported by an Advance Queensland Industry Research Fellowship (AQIRF2020) and acknowledges support from the Queensland University of Technology (QUT) in the form of an Early Career Research Scheme Grant.

Open access publishing facilitated by Queensland University of Technology, as part of the Wiley - Queensland University of Technology agreement via the Council of Australian University Librarians.

### Conflict of Interest

The authors declare no conflict of interest.



## Data Availability Statement

Research data are not shared.

## Keywords

mechanical testing, melt electrowriting, PCL, tissue engineering, tubular scaffolds

Received: February 17, 2022  
Revised: May 23, 2022  
Published online: July 13, 2022

- [1] T. M. Robinson, D. W. Huttmacher, P. D. Dalton, *Adv. Funct. Mater.* **2019**, *29*, 1904664.
- [2] N. T. Saidy, T. Shabab, O. Bas, D. M. Rojas-González, M. Menne, T. Henry, D. W. Huttmacher, P. Mela, E. M. De-Juan-Pardo, *Front. Bioeng. Biotechnol.* **2020**, *8*, 793.
- [3] A. M. van Genderen, K. Jansen, M. Kristen, J. van Duijn, Y. Li, C. C. L. Schuurmans, J. Malda, T. Vermonden, J. Jansen, R. Masereeuw, M. Castilho, *Front. Bioeng. Biotechnol.* **2021**, *8*, 617364.
- [4] P. D. Dalton, *Curr. Opin. Biomed. Eng.* **2017**, *2*, 49.
- [5] P. Mieszczanek, T. M. Robinson, P. D. Dalton, D. W. Huttmacher, *Adv. Mater.* **2021**, *33*, 2100519.
- [6] N. T. Saidy, A. Fernandex-Colino, B. Shiroud Heidari, R. Kent, M. Vernon, O. Bas, S. Mulderrig, A. Lubig, J. Rodriguez-Cabello, B. Doyle, D. W. Huttmacher, E. M. De-Juan-Pardo, P. Mela, *Adv. Funct. Mater.* **2022**, *32*, 2110716.
- [7] T. D. Brown, A. Slotosch, L. Thibaudeau, A. Taubenberger, D. Loessner, C. Vaquette, P. D. Dalton, D. W. Huttmacher, *Biointerphases* **2012**, *7*, 13.
- [8] C. Black, J. M. Kanczler, M. C. de Andrés, L. J. White, F. M. Savi, O. Bas, S. Saifzadeh, J. Henkel, A. Zannettino, S. Gronthos, M. A. Woodruff, D. W. Huttmacher, R. O. C. Oreffo, *Biomaterials* **2020**, *247*, 119998.
- [9] T. Jungst, M. L. L. Muerza-Cascante, T. D. Brown, M. Standfest, D. W. Huttmacher, J. Groll, P. D. Dalton, *Polym. Int.* **2015**, *64*, 1086.
- [10] E. McColl, J. Groll, T. Jungst, P. D. Dalton, *Mater. Des.* **2018**, *155*, 46.
- [11] N. C. Paxton, M. Lanaro, A. Bo, N. Crooks, M. T. Ross, N. Green, K. Tetsworth, M. C. Allenby, Y. Gu, C. S. Wong, S. K. Powell, M. A. Woodruff, *J. Mech. Behav. Biomed. Mater.* **2020**, *105*, 103695.
- [12] T. Jungst, I. Pennings, M. Schmitz, A. J. W. P. Rosenberg, J. Groll, D. Gawlitta, *Adv. Funct. Mater.* **2019**, *29*, 1905987.
- [13] K. Somszor, O. Bas, F. Karimi, T. Shabab, N. T. Saidy, A. J. O'Connor, A. V. Ellis, D. Huttmacher, D. E. Heath, *ACS Macro Lett.* **2020**, *9*, 1732.
- [14] N. C. Paxton, R. Daley, D. P. Forrester, M. C. Allenby, M. A. Woodruff, *Mater. Des.* **2020**, *193*, 108787.
- [15] N. T. Saidy, F. Wolf, O. Bas, H. Keijdener, D. W. Huttmacher, P. Mela, E. M. De-Juan-Pardo, *Small* **2019**, *15*, 1900873.
- [16] M. Castilho, A. van Mil, M. Maher, C. H. G. Metz, G. Hochleitner, J. Groll, P. A. Doevendans, K. Ito, J. P. G. Sluijter, J. Malda, *Adv. Funct. Mater.* **2018**, *28*, 1803151.
- [17] O. Bas, D. D'Angella, J. G. Baldwin, N. J. Castro, F. M. Wunner, N. T. Saidy, S. Kollmannsberger, A. Reali, E. Rank, E. M. De-Juan-Pardo, D. W. Huttmacher, *ACS Appl. Mater. Interfaces* **2017**, *9*, 29430.
- [18] K. A. van Kampen, E. Olaret, I.-C. Stancu, L. Moroni, C. Mota, *Mater. Sci. Eng. C* **2021**, *119*, 111472.
- [19] N. C. Paxton, S. W. K. Ho, B. T. Tuten, J. Lipton-Duffin, M. A. Woodruff, *Macromol. Rapid Commun.* **2021**, *42*, 2100433.
- [20] A. Hrynevich, B. Ş. Elçi, J. N. Haigh, R. McMaster, A. Youssef, C. Blum, T. Blunk, G. Hochleitner, J. Groll, P. D. Dalton, *Small* **2018**, *14*, 1800232.
- [21] A. Hrynevich, I. Liashenko, P. D. Dalton, *Adv. Mater. Technol.* **2020**, *5*, 2000772.
- [22] I. Liashenko, A. Hrynevich, P. D. Dalton, *Adv. Mater.* **2020**, *32*, 2001874.
- [23] M. O'Riordan, "Three Years On, Absorb BVS Still Doesn't Improve Myocardial Blood Flow," <https://www.tctmd.com/news/three-years-absorb-bvs-still-doesnt-improve-myocardial-blood-flow>, (accessed: January 2021).
- [24] Y. Jin, C. Xie, Q. Gao, X. Zhou, G. Li, J. Du, Y. He, *Mater. Des.* **2021**, *197*, 109277.
- [25] Y. Kim, K. Son, J. Lee, *Materials* **2021**, *14*, 6821.
- [26] F. Afghah, C. Dikyol, M. Altunbek, B. Koc, *Appl. Sci.* **2019**, *9*, 3540.
- [27] N. C. Paxton, S. K. Powell, M. A. Woodruff, *Tech. Orthop.* **2016**, *31*, 190.
- [28] O. Bas, B. Gorissen, S. Luposchinsky, T. Shabab, K. Bertoldi, D. W. Huttmacher, *Multifunct. Mater.* **2021**, *4*, 045001.
- [29] Y. Niu, M. Galluzzi, M. Fu, J. Hu, H. Xia, *J. Nanobiotechnol.* **2021**, *19*, 349.
- [30] J. Schindelin, I. Arganda-Carreras, E. Frise, V. Kaynig, M. Longair, T. Pietzsch, S. Preibisch, C. Rueden, S. Saalfeld, B. Schmid, J.-Y. Y. Tinevez, D. J. White, V. Hartenstein, K. Eliceiri, P. Tomancak, A. Cardona, *Nat. Methods* **2012**, *9*, 676.